Multi-Plane Spatially Resolved Phase Structuring Using Optical Communication Modes

Supplementary Material

Vinicius S. de Angelis[1,4*], Maximilian Jeindl[2], Leonardo André Ambrosio[1], David A. B. Miller[3], Federico Capasso[4], and Ahmed H. Dorrah[2,4†]

[1] Department of Electrical and Computer Engineering, São Carlos School of Engineering, University of São Paulo, 400 Trabalhador São-Carlense Ave., 13566-590, São Carlos, São Paulo, Brazil

[2] Department of Applied Physics and Science Education, Eindhoven University of Technology, Eindhoven 5612 AP, The Netherlands

[3] Ginzton Laboratory, Stanford University, Stanford, CA 94305, USA

[4] Harvard John A. Paulson School of Engineering and Applied Sciences, Harvard University, Cambridge, MA 02138, USA

[*] vinicius.angelis@usp.br

[†] a.h.dorrah@tue.nl

Supplementary Note 1: coupling strengths of intrinsic modes

Assume an on-axis source point centered at the source plane emitting a light wave with power P toward the receiving planes as shown in Fig. S1(a). The light intensity at the n-th receiving plane, which has an area $A_n = X_n Y_n$, is:

$$I_n = \frac{P}{A_n} = \frac{P}{(p_r-1)^2 4\lambda^2 [1+(n-1)(L/L_0)]^2} = \frac{I_1}{[1+(n-1)(L/L_0)]^2}, \tag{S1}$$

in which $I_1 = P/[4\lambda^2(p_r-1)^2]$ is the light intensity at the first plane. The coupling strengths of the intrinsic modes decay from plane to plane with the same inverse-square dependence as the intensity, i.e.:

$$|s_{\text{int},n}|^2 = \frac{|s_{\text{int},1}|^2}{[1+(n-1)(L/L_0)]^2}, \tag{S2}$$

as shown in Fig. S1(b) for different values of L/L_0, in which the dots represent the values evaluated from Eq. S2. This indicates that these modal strengths are simply proportional to the light intensities prescribed in Eq. S1.

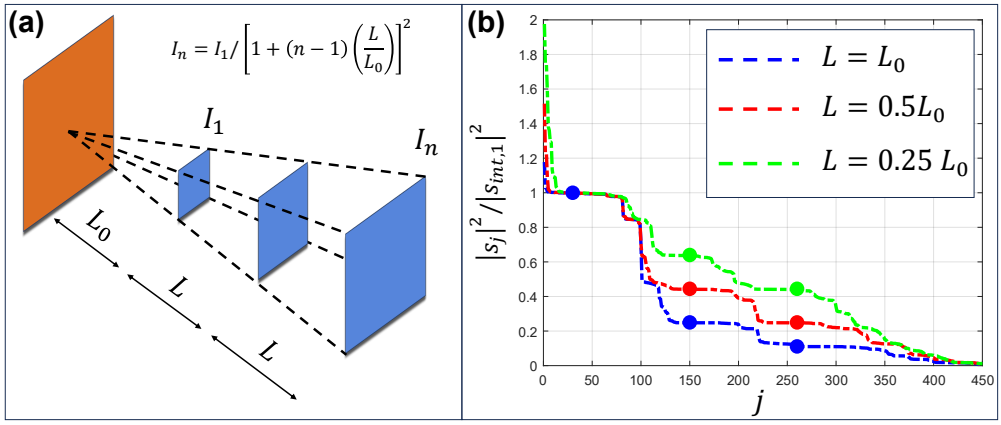

Fig. S1. Coupling strengths of intrinsic modes. **(a)** Intensity decay from an on-axis source point centered at the source plane. **(b)** The coupling strengths of intrinsic modes also decay with the same inverse-square dependence. The dots represent the modal strengths computed from this dependence (see Eq. S2).

Supplementary Note 2: Phase retrieval algorithm

A variation of the SBMIR algorithm by Almoro and Pedrini [1] was implemented in Matlab. A Fresnel propagation formalism was used to propagate the complex field amplitudes between different planes. The SBMIR reconstructs the phase and amplitude of fields along the propagation direction using intensity measurements acquired at N planes. High and low resolution ranges in propagation direction were defined, where areas close to the designed planes have more measurement points. The recorded frame size was chosen to encompass the region containing features reasonably above the noise floor. Additionally, 12 exposures were binned into a single measurement frame, and each data point consists of several such measurement frames. An averaged dark frame of the camera at the same camera settings was subtracted from measurements before the phase retrieval. Pixel values that are negative after background subtraction are set to zero to avoid unphysical intensities.

First, a starting plane with measured intensity I_k is selected, and the corresponding complex field is initialized as $A_k = \sqrt{I_k} \cdot \exp\left(i\Phi_{k,\text{initial}}\right)$, with $\Phi_{k,\text{initial}}$ chosen as a pixel-wise random phase. Afterwards, the iterative algorithm starts with the assumed phase and amplitude A_k numerically propagated a distance $z_m - z_k$ to a different measurement plane, as illustrated in Fig. S2. Here the field amplitude $A_m \rightarrow \sqrt{I_m} \cdot \exp\left(i\Phi_m\right)$ is replaced using the measured intensity, while the propagated phase $\Phi_m = \text{angle}(A_{m,\text{propagated}})$ is kept. Next, A_m is propagated back $z_k - z_m$ to the position of the reference plane, where again the amplitude is replaced while the phase is kept. This yields the phase-amplitude $A_k = \sqrt{I_k} \cdot \exp\left(i\Phi_{k,\text{propagated}}\right)$. For the next step, a new plane at z_l is selected and the procedure is repeated until all planes of interest have been included, completing a single iteration. A fixed number of iterations is performed, after which convergence is assessed. The iteration counts for the different measurements, along with selected quality metrics, are reported in Table S1.

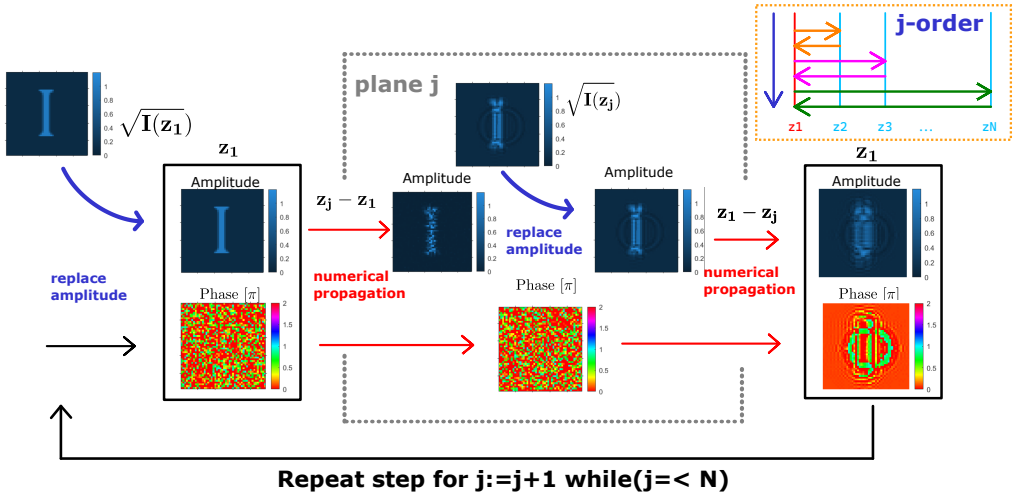

Fig. S2. Sub-step of SBMIR iteration step. Here z_1 is the first plane along the propagation direction and $z_j < z_{j+1}$ for all j. The inset on top right indicates the order in which the planes are included within a single iteration along the incremental propagation direction.

The first designed plane, which lies at the focal distance of the second lens of the $4f$ system, was chosen as the reference plane. Each sub-cycle starts and ends at that plane as shown in Fig. S2. The subsequent planes were selected incrementally along the propagation direction. Choosing the first plane as a reference was done for predictability, even though it implies a higher weight towards the first plane for the reconstructed fields. For computational efficiency, the iterations, which rely heavily on Fast-Fourier-Transforms, were done on a GPU. Due to memory limitations, only a part of the measurement could be included in the iterations. Using the first approximately 100 planes, along the propagation direction, for the phase retrieval yielded more stable convergence than including only every second plane of the entire propagation range or taking the last 100 planes. The result of the phase retrieval was manually evaluated after a fixed number of iterations and is summarized in Table S1. Supplementary Video 2 presents the measured intensity and retrieved phase of all measured planes for the phase structuring case

Table S1. Phase retrieval metrics for each measured result. RMS is the root mean square error comparing intensity measurement and retrieved squared amplitude. $I_{\max}$ is the maximum pixel value over all planes. N_{iter} is the number of SBMIR iterations performed. HR and LR refer to the adopted high and low resolution ranges in propagation direction. The former were set to areas close to the designed planes. Start and end indicate the index of the first and the last plane used in the phase retrieval. The start index is always the highest index and corresponds to the first measured plane in propagation direction. d_{meas} is the total propagation distance covered by the measurement and d_{SBMIR} is the percentage of that which lies between the start and end indices used for the phase retrieval. N_F is the number of exposures per measurement point.

Reference	RMS/$I_{\max}$	N_{iter}	HR (LR) (mm)	d_{meas} (mm)	start	end	d_{SBMIR} (%)	N_F
Fig 4 (a,b)	0.01274	400	0.2 (1.0)	1.500E+01	287	120	0.532	36
Fig 4 (c,d)	0.01041	800	0.2 (1.0)	1.500E+01	287	120	0.532	48
Fig 5 (d)	0.01010	800	0.2 (1.0)	1.500E+01	247	100	0.713	36
Fig 5 (e)	0.01227	800	0.2 (1.0)	1.500E+01	247	100	0.713	36
Fig S9	0.00786	800	0.25 (0.25)	1.020E+01	409	190	0.537	12
Fig 6	0.00739	50	0.2 (1.0)	1.499E+01	295	145	0.510	36

shown in Figs. 4(c-d).

For Fig. S9 (non-paraxial case), some parameters differ. No background subtraction was executed, instead a constant value of 1 was subtracted from all pixels, to adjust the reported camera intensity range from [1,4095] to [0,4094]. Additionally, the stage positioning and $4f$ adjustment was different, as the fields encoded on the SLM were based on the wave solution computed at $z = 0.75L_0$, requiring a different spacing of translation stage relative to the second $4f$ lens. The collimation here was only tested visually, leading to looser alignment of the $4f$ system in the propagation direction and thus a deviation to the designed magnification.

Due to memory constraints, every frame is captured as a multi exposure of 12 image acquisitions. Multiple such frames may be recorded for any position to increase the number included in the average. However, to conserve memory, only the highest standard deviation of all pixels in the frame is recorded. Additionally, the RMS of the pixel standard deviations of all pixels within a frame is calculated as:

$$RMS(\sigma_{pixel}) = \sqrt{\sum_{i}^{N} \frac{(\sigma_{\text{pixel},i})^2}{N}}. \tag{S3}$$

The maximum of all frames within a measurement for both the maximum pixel standard deviation and the RMS value of the frame is shown in Table S2. The frame-to-frame intensity fluctuations at the same measurement plane remain below 6.6% of the maximum intensity across all configurations. Camera acquisition noise for no illumination (Background in Table S2) shows a maximal $\sigma_{\max} < 7$, implying a low camera influence on the experimental noise. The main experimental sources of uncertainty are air movement and mechanical vibrations from the translation stage, which were mitigated through cable management, a short pause after each stage movement, and stray light shielding.

Table S2. Measurement noise statistics out of 12 frame averages. Highest pixel standard deviation of entire measurement and highest RMS of all frames in the measurement are reported to give an upper bound to noise. I_{max} is the maximum averaged pixel intensity within a measurement. Background: metrics of camera acquisition noise for no illumination (background).

	Measurement				Background			
Ref.	σ_{max}	RMS_{max}	I_{max}	σ_{max}/I_{max}	σ_{max}	RMS_{max}	I_{mean}	I_{max}
Fig.4(a,b)	2.06E+02	7.6	3.118E+03	6.6E-02	6.2	0.033	1.01	4.1
Fig.4(c,d)	1.87E+02	6.3	3.459E+03	5.4E-02	6.0	0.034	1.01	3.6
Fig.5(d)	1.26E+02	5.4	3.697E+03	3.4E-02	6.2	0.029	1.01	4.5
Fig.5(e)	1.33E+02	7.2	4.009E+03	3.3E-02	5.6	0.028	1.01	3.8
Fig.S9	1.06E+02	3.7	2.821E+03	3.8E-02	5.8	0.029	1.01	3.6
Fig.6	1.40E+02	7.4	3.149E+03	4.5E-02	5.8	0.109	1.01	4.1

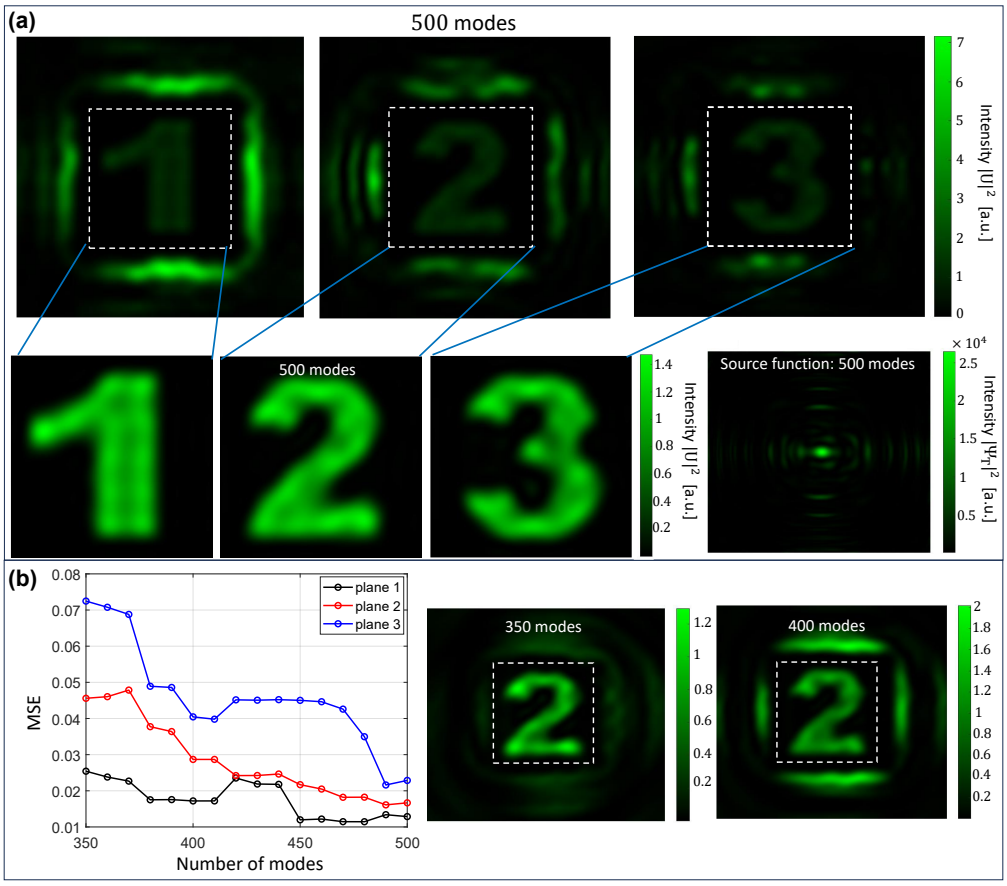

Fig. S3. Reconstruction accuracy as a function of the number of modes included in the synthesis. For the example of Fig. 2(b) we incorporate the first 500 modes in an attempt to fully reconstruct the flat-topped profiles of the target digits. **(a)** Calculated source function and resulting wave at the three receiving planes. The improvement in reconstruction accuracy is afforded by a substantial increase in source amplitudes. This high energy remains largely confined outside the target planes due to the tunneling-like escape behavior of these weakly coupled modes. The dashed white squares highlight the dimensions of the target planes. **(b)** Mean squared error (MSE) versus number of modes. While the MSE decreases (e.g., from 0.0456 at 350 modes to 0.0287 at 400 modes in the second plane), the intensity outside the target region increases significantly, reaching values up to 2× higher than inside the target.

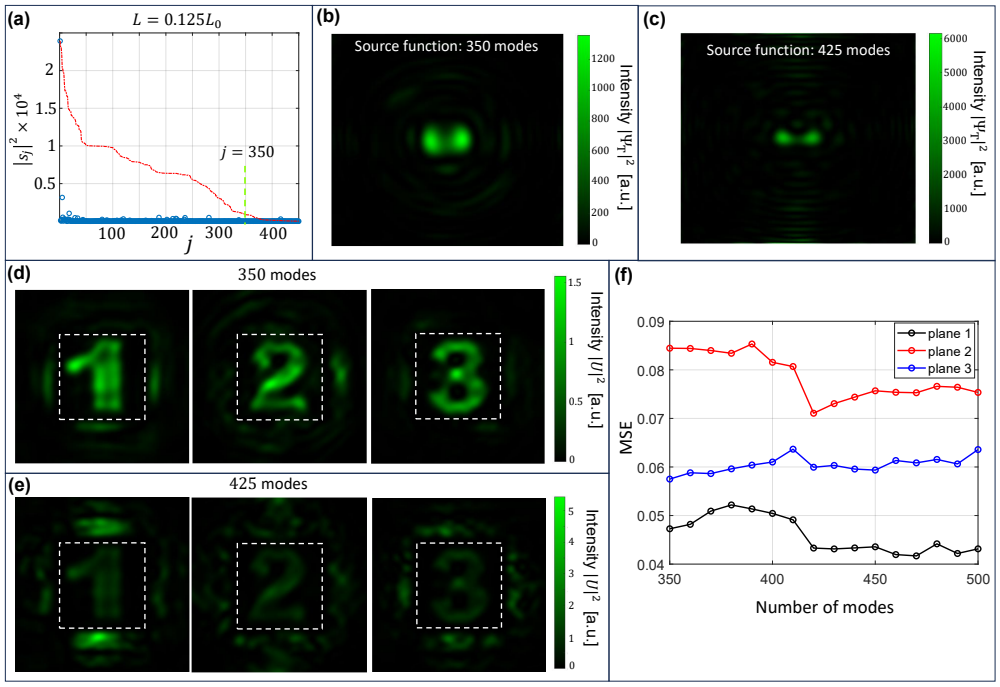

Fig. S4. Structuring arbitrary light wave profiles for smaller separation distances between the target planes. **(a)** Projection of the target patterns (intensity profiles of the binary digits '1','2' and '3') onto the receiving basis (blue circles) for $L = 0.125L_0$. Calculated source function computed from **(b)** the first 350 modes and from **(c)** the first 425 modes. **(d-e)** Reconstructed intensity distributions for these cases. **(f)** Reconstruction accuracy at the target planes as a function of the number of modes included in the synthesis. For reduced plane separation, the improvement in reconstruction accuracy obtained by incorporating weakly coupled modes is significantly diminished.

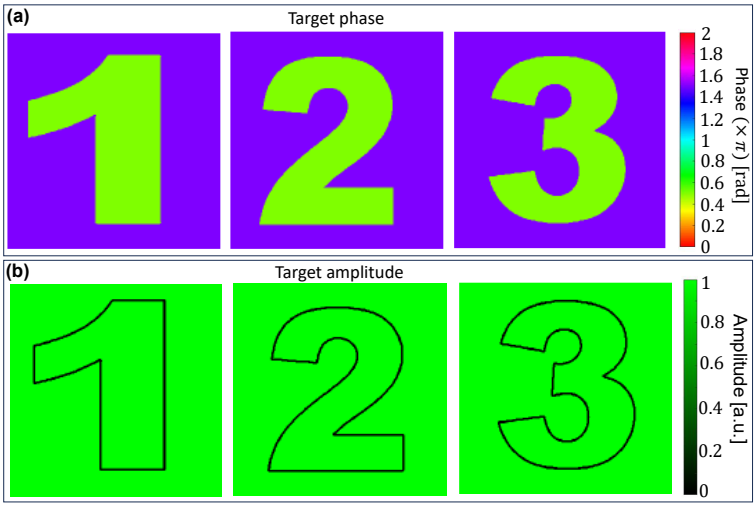

Fig. S5. Target phase and amplitude profiles to create 2D sheet singularities. **(a)** A π-phase discontinuity at the prescribed singularity locations is assigned by defining a phase of $\pi/2$ radians inside the singularity contour and a phase of $3\pi/2$ radians outside. **(b)** Along each singularity contour the amplitude is set to zero while a uniform unit value amplitude is set elsewhere.

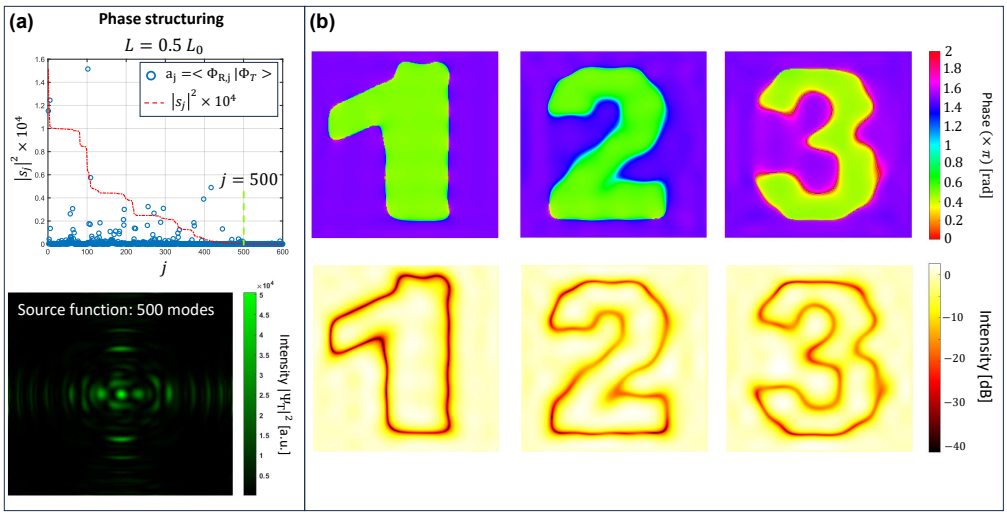

Fig. S6. Mathematically exact phase-sheet singularities. Due to finite source aperture, mathematically exact phase singularities can only be achieved by incorporating weakly coupled modes. **(a)** For the example of Fig. 2(e) the source function is computed from the first 500 modes. **(b)** The high-energy source function due to the incorporation of weakly coupled modes results in singular points with intensity as low as -41 dB across all planes.

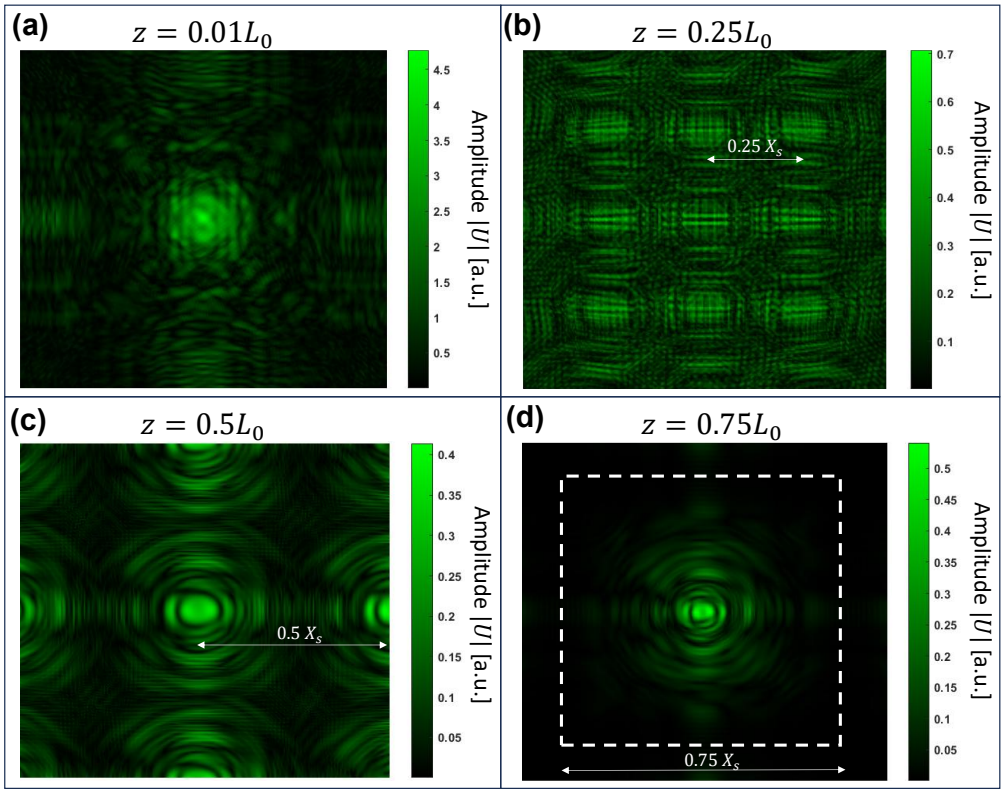

Fig. S7. Longitudinal evolution of the wave amplitude propagated from the source plane. At short distances, **(a)** $z = 0.01L_0$ and **(b)** $z = 0.25L_0$, the field exhibits strong reactive near-field structure associated with evanescent spatial-frequency components. These features decay with propagation and by **(c)** $z = 0.5L_0$ the field is mostly dominated by propagating components. However, at this distance, diffraction orders still spatially overlap. **(d)** From about $z = 0.75L_0$, the wave propagated from the source plane is a smooth propagating field with no contributions from higher diffraction orders, suitable for SLM encoding. The distances highlighted in white indicate the separation distances between the diffraction orders.

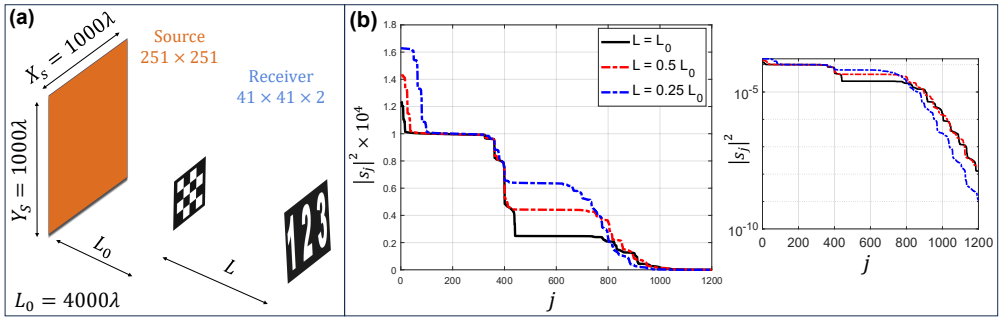

Fig. S8. Coupling strengths for larger receiving arrays. **(a)** Configuration of Fig. 5(a) analyzed for distinct values of the separation distance between the receiving planes. **(b)** Coupling strengths for distinct values of the ratio L/L_0 on a linear and a logarithmic scale. For these receiving arrays the total number of strongly coupled modes begins to decrease at $L = 0.25L_0$.

Table S3. Quantitative metrics for experimentally reconstructed intensity and phase profiles in Fig. 5(d–e).

	Intensity structuring			Phase structuring		
Plane	MSE	SBR	C	MSE	$\sigma_{\text{int}}(\times\pi)$	$\sigma_{\text{out}}(\times\pi)$
1	0.1469	13.35	0.5338	0.0790	0.1336	0.0835
2	0.1086	5.847	0.5596	0.2498	0.2765	0.5040

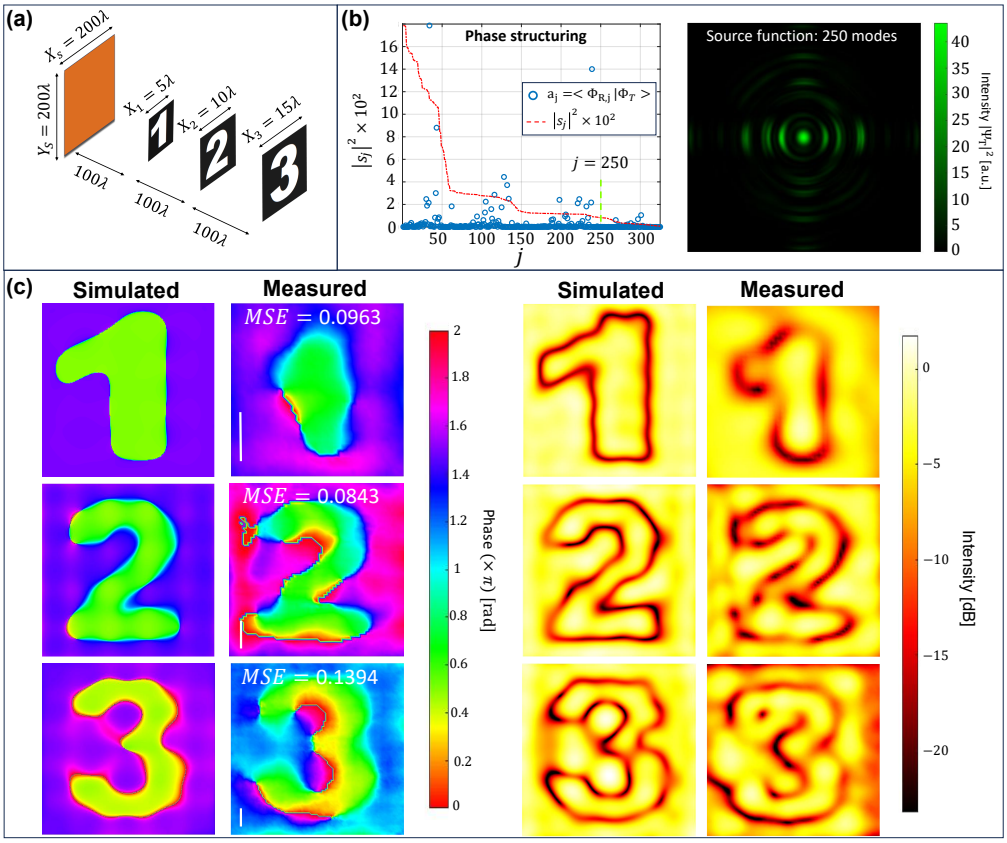

Fig. S9. Structuring light waves in the non-paraxial regime. **(a)** A configuration of target planes and source aperture in this regime. **(b)** Coupling strengths (red dashed line) and projection (blue circles) of the same target phase profiles as in Fig. 2. The source function is computed from the first 250 well-coupled modes. To facilitate the measurements, the wave solution is computed at $z = 0.75L_0$ (instead of at $z = L_0$) to increase the separation distances between the measured planes. **(c)** Measured retrieved phase profiles and intensity (in dB) at the target planes. Mean squared errors between measured and target phase profiles are shown in white. Scale bars (vertical white lines) represent 24 μm. The second and third planes are longitudinally spaced by 47.75 mm and 95 mm from the first plane.

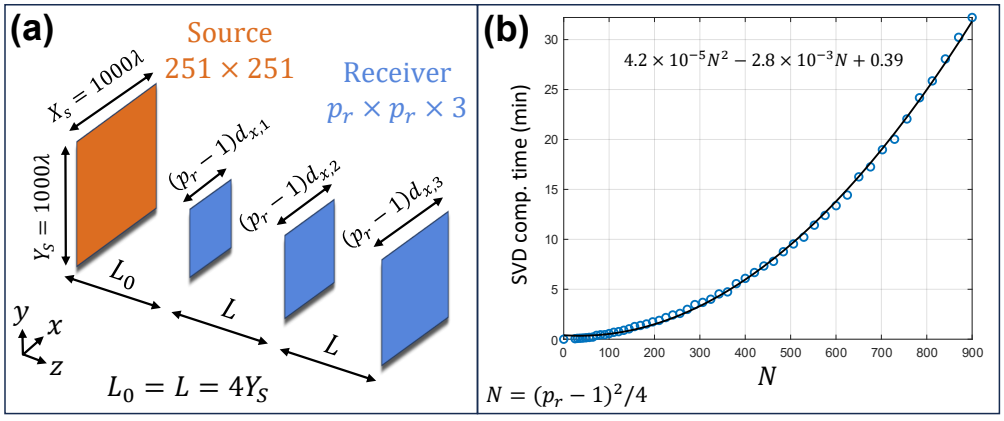

Fig. S10. SVD computation cost and scalability. (a) For a given source aperture, the SVD computation cost is evaluated as a function of the number of strong modes N supported in each plane. This number is increased with the array size $p_r \times p_r$ of the receiving planes, $N = (p_r - 1)^2/4$. **(b)** The computation cost grows approximately quadratically with the number of modes N. The economy-size SVD was performed in a dedicated server with processor Intel(R) Xeon(R) CPU ES-2690 0 @ 2.90 GHz.

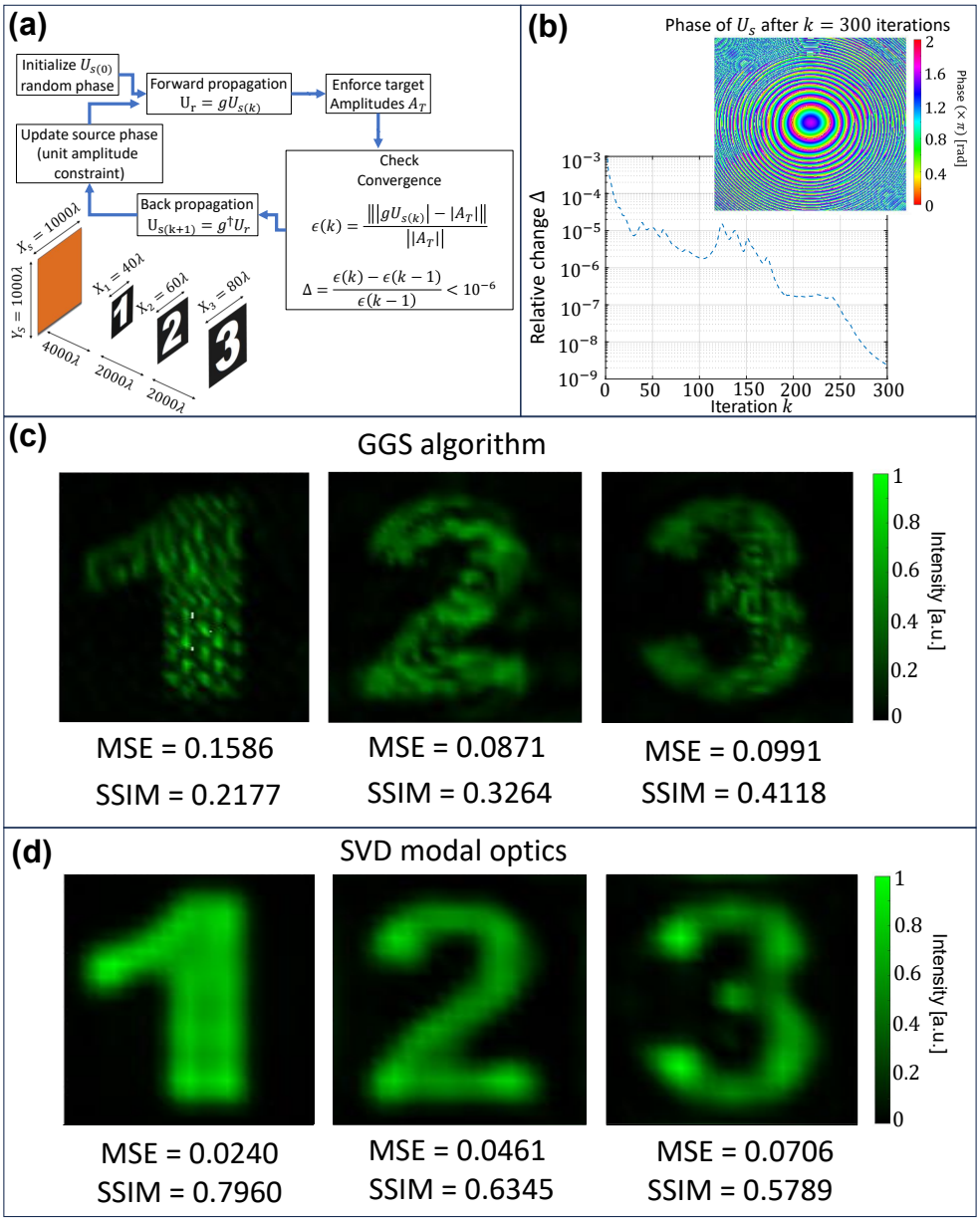

Fig. S11. Comparison with GGS algorithm. The GGS algorithm is applied to the configuration of Fig. 2(b) for the intensity reconstruction of the target digits '1', '2' and '3'. **(a)** Flowchart of the iterative GGS procedure. The source is initialized with a random phase, and forward/backward propagation is performed using the Green's function kernel g (Eq. 2). To match the energies of all depth layers, the normalized target amplitude A_T at each n-th plane is multiplied by $[1 + (n-1)(L/L_0)]^2$. **(b)** After about 200 iterations, the algorithm reaches stagnation with relative change in reconstruction $\Delta < 10^{-6}$. Inset shows the phase at the source plane after $k = 300$ iterations. **(c)** Simulated reconstructed intensity profiles after 300 iterations, with corresponding MSE and SSIM values. **(d)** Simulated reconstruction using the first 357 communication modes for the same configuration.

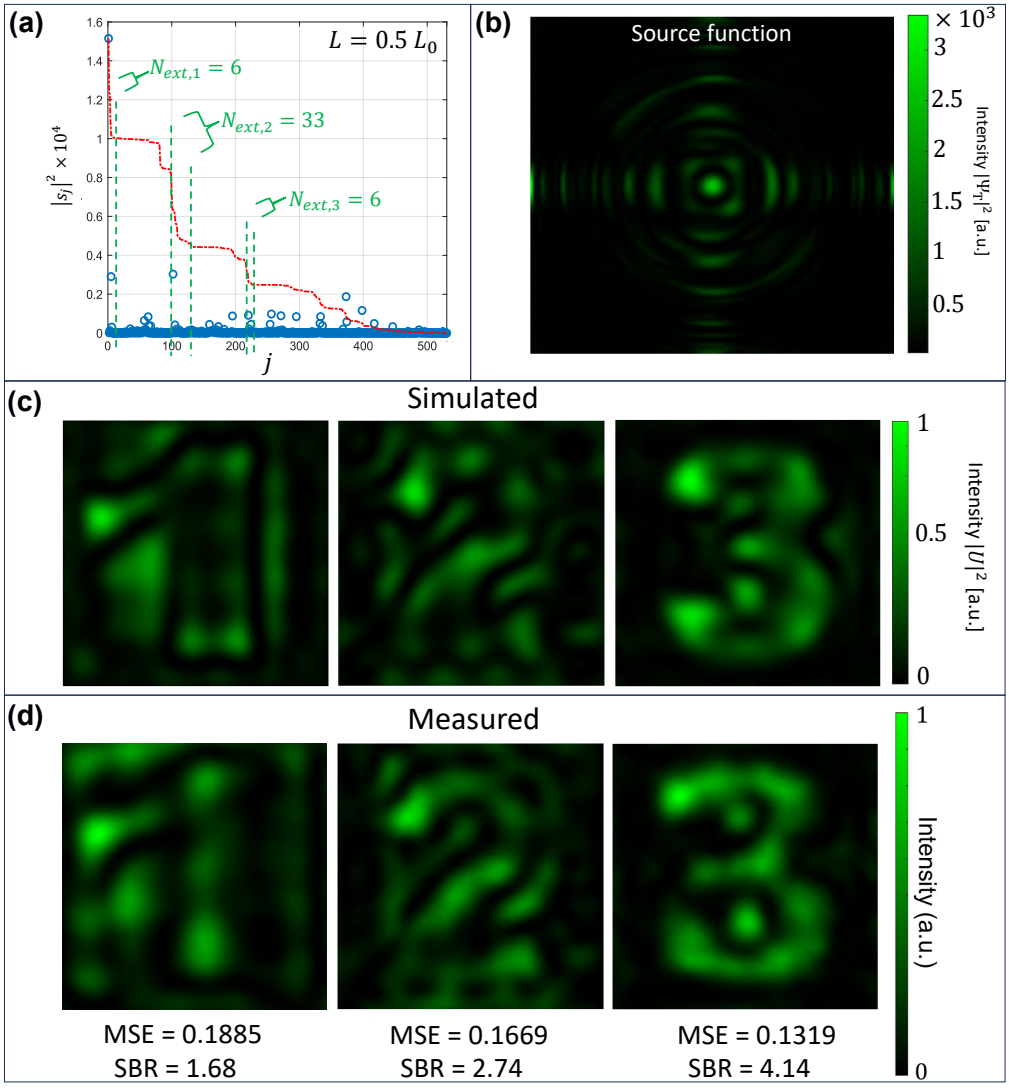

Fig. S12. Excluding extrinsic modes in light wave synthesis. **(a)** For the configuration in Fig. 2(b), the intensity profiles of the digits '1', '2' and '3' are projected onto the receiving planes (blue circles), with the range and number of extrinsic modes indicated (green dashed lines). **(b)** Source function computed without extrinsic modes. **(c)** Simulated wavefields at the target planes, showing degraded reconstruction and increased inter-plane crosstalk. **(d)** Experimental measurements with corresponding mean squared error (MSE) and signal-to-background ratio (SBR) metrics.

REFERENCES

1. P. Almoro, G. Pedrini, and W. Osten, "Complete wavefront reconstruction using sequential intensity measurements of a volume speckle field," Appl. Opt. **45**, 8596–8605 (2006).